Applied Surface Science 712 (2025) 164190

Contents lists available at ScienceDirect

Applied Surface Science

journal homepage: www.elsevier.com/locate/apsusc

Full Length Article

Highly selective ammonia detection by SnS_2 nanosheets functionalized $Ti_3C_2T_x$

Lizhai Zhang [a,b,c,e,*], Jiayuan Xu [d], Xinyu Lei [a], Henghui Sun [a], Taotao Ai [a,*], Fei Ma [b,e], Paul K Chu [c,**]

[a] School of Materials Science and Engineering, Shaanxi University of Technology, Hanzhong 723001 Shaanxi, China
[b] State Key Laboratory for Mechanical Behavior of Materials, Xi'an Jiaotong University, Xi'an 710049 Shaanxi, China
[c] Department of Physics, Department of Materials Science and Engineering, and Department of Biomedical Engineering, City University of Hong Kong, Tat Chee Avenue, Kowloon, Hong Kong, China
[d] Shaanxi Engineering and Technology Research Center for Industrialization of Natural Active Products, Shaanxi University of Technology, Hanzhong, Shaanxi 723001, China
[e] College of Physics and Information Technology, Shaanxi Normal University, Xi'an 710062 Shaanxi, China

ARTICLE INFO

Keywords:
SnS_2
$Ti_3C_2T_x$ MXene
Heterojunction
NH_3 detection
Selectivity

ABSTRACT

SnS_2 is very promising for next-generation gas sensors due to the abundant edge-exposed sites, large surface-to-volume ratio, and high charge carrier mobility. However, SnS_2 suffers from low response and poor selectivity in gas sensing. In this paper, the self-activated SnS_2 gas sensor functionalized with $Ti_3C_2T_x$ is designed and fabricated to monitor NH_3 at room temperature (RT) in daily life. The response of SnS_2 and $Ti_3C_2T_x$ composites to 500 ppm NH_3 is about 86.35 % at RT, which is enhanced by 43.82 % and 38.33 % in comparison with pure SnS_2 and $Ti_3C_2T_x$, respectively. The SnS_2-functionalized $Ti_3C_2T_x$ micropatterns show high selectivity to NH_3 and a low detection limit of 143 ppt. Density-functional theory (DFT) calculations reveal that the $SnS_2/Ti_3C_2T_x$ heterojunction provide the additional active sites for NH_3 adsorption, enhancing the absorption and diffusion capabilities of NH_3. In addition, the remarkable metallic conductivity of $Ti_3C_2T_x$ MXene ensures efficient electron transfer to improve the sensing characteristics.

1. Introduction

Meat products such as beef, pork, and fish decay rapidly under ambient conditions because the high protein content provides a suitable environment for microbial growth [1]. As meats rot, the microbial activity increases, resulting in the production of various gases such as ammonia, hydrogen sulfide, and volatile organic compounds [2]. Hence, accurate and sensitive detection of ammonia (NH_3) can monitor food quality. Furthermore, NH_3 serves as a biomarker to monitor kidney and liver disorders, and early detection can prevent cancer [3–6]. Therefore, real-time detection of NH_3 is important to ensure public safety, monitor food quality, and develop disease diagnostics.

Because of the abundant edge-exposed sites, large surface-to-volume ratio, and high carrier mobility, SnS_2 has attracted significant research attention, especially with respect to NH_3 gas sensing [7–13]. *Xiong et al.* have prepared SnS_2 nanoflowers hydrothermally and observed excellent response to NH_3 at 200 ℃ as well as short response and recovery times [11]. *Zhang et al.* have prepared 3D SnS_2 hierarchical micro-flowers by a hydrothermal method with $ZnSn(OH)_6$ hollow nanospheres as the precursor and found a good response to 50 ppm NH_3 at 160 ℃ with response and recovery times of 4 s and 15 s, respectively [12]. Theoretical calculations indicate that NH_3 molecules chemisorb on S-vacancy SnS_2 monolayers by strong covalent bonds and behave as charge donors [13]. Unfortunately, gas sensors based on SnS_2 need a high working temperature [7–10] and the restacking and agglomeration of 2D SnS_2 during gas adsorption and desorption diminish the surface area and number of active sites, thereby degrading the response and selectivity [7–12].

To enhance the response and selectivity of SnS_2, constructing heterojunction of SnS_2 and other 2D materials is the effective strategy [13–17]. On one hand, the heterostructures could integrate the structural advantages of multiple components and avoid self-stacking of SnS_2

* Corresponding authors at: School of Materials Science and Engineering, Shaanxi University of Technology, Hanzhong 723001, Shaanxi, China.
** Corresponding author.
E-mail addresses: zhanglizhai0512@snut.edu.cn (L. Zhang), aitaotao0116@126.com (T. Ai), paul.chu@cityu.edu.hk (P.K. Chu).

https://doi.org/10.1016/j.apsusc.2025.164190
Received 26 May 2025; Received in revised form 16 July 2025; Accepted 28 July 2025
Available online 29 July 2025

nanosheets. On the other hand, the van der Waals interactions between 2D/2D heterostructures facilitate interfacial charge transfer, consequently avoiding the lattice mismatch encountered by semiconductor heterostructures [18–20]. In addition, the construction of heterostructures can also effectively increase the number of adsorption sites and improve the gas sensing response and selectivity [18–20]. For example, *Liao et al.* have synthesized SnS_2 and graphene composites by the hydrothermal method and observed excellent NH_3-sensing properties at room temperature (RT). The response of SnS_2/graphene composites to 100 ppm NH_3 is enhanced by 36 % and 28.63 % at RT in comparison with pure SnS_2 and graphene, respectively [14]. $Ti_3C_2T_x$, a new class of 2D materials, has a unique layered structure, adjustable electrical properties, and abundant terminal groups [21–24]. The accordion-like delaminated layer structure of $Ti_3C_2T_x$ provides abundant edge-exposed sites for gas adsorption and expedites charge transport during gas sensing [21–24]. Hence, if the SnS_2 is deposited on the surface of $Ti_3C_2T_x$, the NH_3-sensing performance at RT may be effectively enhanced.

Herein, a composite comprising SnS_2 and $Ti_3C_2T_x$ is prepared by a hydrothermal method. The SnS_2 nanosheets on $Ti_3C_2T_x$ could inhibit restacking of SnS_2 and oxidation of $Ti_3C_2T_x$. The $Ti_3C_2T_x$ serves as template for growth of SnS_2 nanosheets and generates interfacial sites for NH_3 gas adsorption. The composites show the enhanced NH_3 sensing response ranging from 15.8 % to 86.35 % as the NH_3 concentration is increased from 10 to 500 ppm at RT. More importantly, it has excellent selectivity, stability, fast response and recovery rate. First-principles calculation is conducted to elucidate the enhanced NH_3-sensing mechanism at RT.

2. Experimental Section

2.1. Synthesis of SnS_2 and $Ti_3C_2T_x$ composites

HF-etched $Ti_3C_2T_x$ was placed in 30 mL deionized water and magnetically stirred for 60 min, followed by addition of 0.25 g of $SnCl_4{\cdot}5H_2O$ and 0.35 g of thiourea. After magnetic stirring for 120 min, the solution was introduced into a 50 mL Teflon-lined stainless-steel autoclave and treated to 200 °C for 24 h. After cooling to RT, the precipitate was washed three times with ethanol and deionized water, centrifuged at 6,000 rpm, and dried at 60 °C in vacuum overnight. To study the effects of $Ti_3C_2T_x$ contents, solutions with 0.19 wt% (0.49 mg), 0.48 wt% (1.2 mg), 1.32 wt% (3.3 mg), and 2.12 wt% (5.3 mg) $Ti_3C_2T_x$ were prepared, and the samples were designated as Sn-Ti-a, Sn-Ti-b, Sn-Ti-c, and Sn-Ti-d, respectively (Fig. 1). The pure SnS_2 sample was prepared by the same method without $Ti_3C_2T_x$. In order to inhibit the oxidation of $Ti_3C_2T_x$ during the hydrothermal process, N_2 was bled into the solution to purge dissolved oxygen before reaction.

2.2. Characterization

The crystal structure was analyzed by X-ray diffraction (XRD, Bruker D8 Advance) using Cu K_α radiation ($\lambda = 1.5418$ Å), and Raman spectra were acquired from SnS_2, $Ti_3C_2T_x$, and $SnS_2/Ti_3C_2T_x$ composites with 532 nm laser excitation (LabRAM HR Evolution). The morphology and microstructure were observed by field-emission scanning electron microscopy (FE-SEM, Zeiss Gemini SEM 500) and transmission electron microscopy (TEM, JEM-2100F Plus). The elemental composition and chemical states of $SnS_2/Ti_3C_2T_x$ composites were determined by the X-ray photoelectron spectroscopy (Thermo Fisher ESCALAB Xi +).

2.3. Fabrication of gas sensor and Measurement

To fabricate the gas sensor, a viscous slurry was prepared by grinding the mixture consisting of 1 mg of the sample in 0.1 mL of deionized water. The sensing film was prepared by coating 0.02 mL of the slurry onto the surface of a commercial Au electrode obtaining a sensing film of 100 μm thickness. The static testing system (CGS-8HP) was used to measure the gas sensing properties. Different amounts of liquid ammonia were injected onto a heater placed inside the sensing chamber using the Hamilton microliter syringe. The gas concentration (C, ppm) was attained by Eq. (1):

$$C = \frac{22.4 \times \rho \times d \times V_s}{M \times V}, \tag{1}$$

where, V_s is the volume of liquid (mL), V is the volume of the chamber (mL), M is the molecular weight of gas (g), ρ is the liquid purity (wt%), and d is the liquid density (g/cm^3). The response to resistance change is derived from Eq. (2):

$$S = \frac{|R_a - R_g|}{R_a} \times 100, \tag{2}$$

where R_a and R_g denote the sensor resistances in air and NH_3,

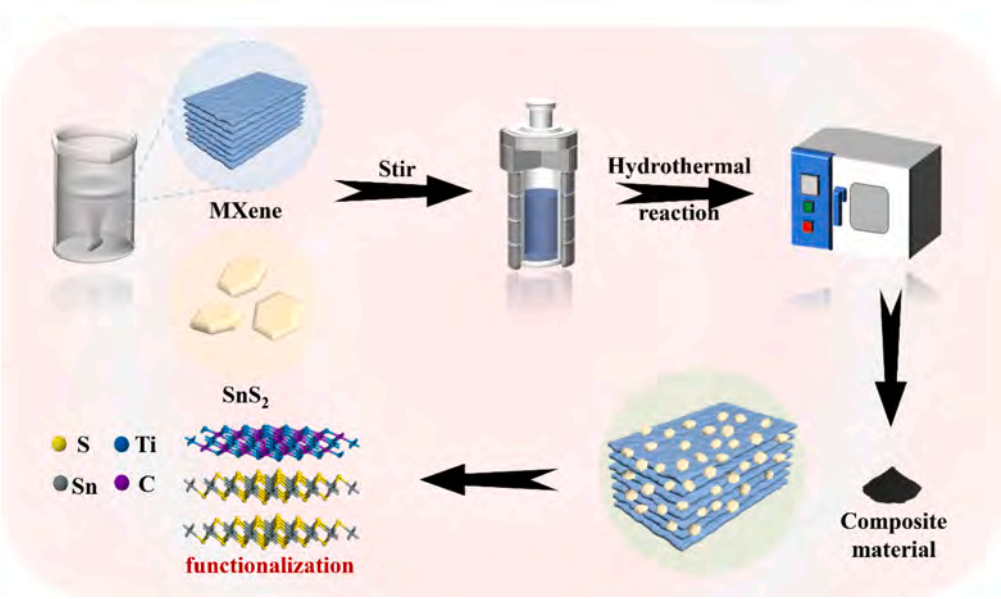

Fig. 1. Schematic diagram of the preparation of SnS_2 and $Ti_3C_2T_x$ composites.

respectively. The response and recovery time correspond to a 90 % change of the total resistance. The environmental humidity was changed by injection of water into a heater placed inside the sensing chamber using the hamilton microliter syringe.

2.4. Theoretical calculation

The theoretical calculations were performed with the Vienna Ab Initio simulation package (VASP) by the projector augmented wave method for the core region and a planewave kinetic energy cutoff of 500 eV [25–27]. The generalized gradient approximation (GGA) in the form of Perdew-Burke-Ernzerhof (PBE) was used for the exchange–correlation potentials. The vacuum layer of the slab models was set to be at least 20 Å in the Z direction to isolate the surface and prevent interactions between two periodic units. The $3 \times 3 \times 1$ and $5 \times 5 \times 1$ Monkhorst-Pack sampled k-point grid was employed in structure optimization and calculation of density of states, respectively. The convergence of energy and residual force on each atom was smaller than 1×10^{-4} eV and 0.05 eV $Å^{-1}$, respectively. The adsorption energy (E_{ads}) of a gas molecule was calculated by Eq. (3):

$$E_{ads} = E_{Sensor+gas} - E_{Sensor} - E_{gas}, \quad (3)$$

where $E_{Sensor+gas}$ is the energy of the sensor and gas, while E_{Sensor} and E_{gas} are the energy of the individual sensor and gas molecule, respectively.

3. Results and Discussion

3.1. Structural Characterization

The x-ray diffraction (XRD) is performed to determine the crystal structure of Ti_3AlC_2, $Ti_3C_2T_x$, SnS_2 and $SnS_2/Ti_3C_2T_x$ composites. In Fig. 2, compared with Ti_3AlC_2, the (002) and (004) peaks of $Ti_3C_2T_x$ MXene were shifted to smaller angles, indicating formation of laminated microstructure after HF etching. In addition, the diffraction peaks of original Ti_3AlC_2 MAX were vanished, which suggested that Al atoms have been removed. Finally, the diffraction peaks at about 14.98°, 28.22°, 32.12°, 41.84°, 49.94°, and 52.48° correspond to the (001), (100), (101), (102), (110), and (111) crystal plane of hexagonal SnS_2 (JCPDS card no. 22–0951). The characteristic peaks of SnS_2 are observed from $SnS_2/Ti_3C_2T_x$ composites, but not $Ti_3C_2T_x$, due to the small amount of $Ti_3C_2T_x$ in the composites. The Raman scattering spectra of Ti_3AlC_2, $Ti_3C_2T_x$, SnS_2 and $SnS_2/Ti_3C_2T_x$ composites are displayed in Fig. 3. In

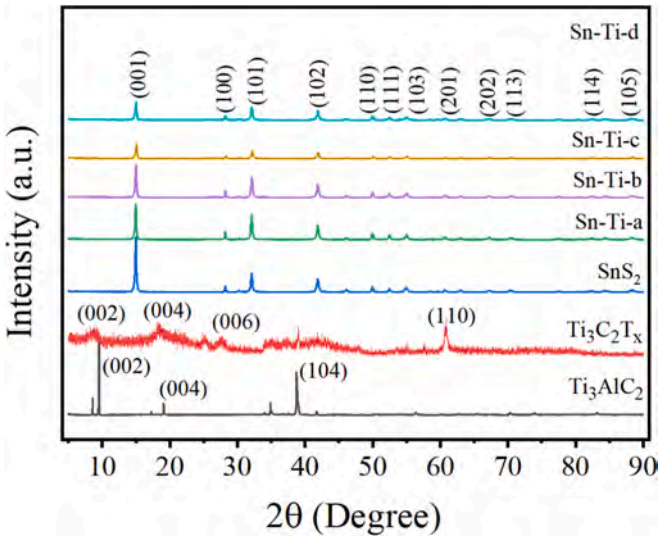

Fig. 2. The XRD spectra of Ti_3AlC_2, $Ti_3C_2T_x$, SnS_2, Sn-Ti-a, Sn-Ti-b, Sn-Ti-c, and Sn-Ti-d.

the Raman spectrum of Ti_3AlC_2, the peak at about 286.9 cm^{-1} corresponds to the vibrational mode of Ti-Al. The peak at about 205.6 cm^{-1} confirms formation of $Ti_3C_2T_x$. For the SnS_2, the peak at about 312.7 cm^{-1} corresponds to the A_{1g} vibrational mode of Sn–S. As for $SnS_2/Ti_3C_2T_x$ composites, the A_{1g} vibrational peak slightly blueshifts to 314.5 cm^{-1}, suggesting charge transfer between SnS_2 and $Ti_3C_2T_x$ at interface [22–24,28].

The morphologies of SnS_2, $Ti_3C_2T_x$, and $SnS_2/Ti_3C_2T_x$ composites are characterized by scanning electron microscopy (SEM). As illustrated in Fig. 4(a–c), SnS_2 has a hexagonal structure with the average thickness and length of SnS_2 nanosheets being about 94 nm and 560 nm, respectively. Fig. 4(d–f) present the SEM micrographs of $Ti_3C_2T_x$ revealing an accordion-like multilayer nanosheet structure. The small granular $Ti_3C_2T_x$ is attached to the surface of accordion-like structure stemming from nanosheet damage during sonication and stirring. Fig. 4 (g–i) present the SEM morphologies of $SnS_2/Ti_3C_2T_x$ composites with different magnifications. Compared with $Ti_3C_2T_x$ and SnS_2, hexagonal SnS_2 is prepared on the edge and surface of $Ti_3C_2T_x$ in the composite to facilitate formation of heterointerfaces and provide abundant adsorption sites for NH_3 molecular. The average length of SnS_2 nanosheets in the composite is about 476 nm. As shown in Fig. 4(j–l), Sn and S are uniformly distributed on the surface of $Ti_3C_2T_x$. The results show that SnS_2 nanosheets are grown on the surface of $Ti_3C_2T_x$ to form compact heterogeneous interfaces with improved charge transfer. In addition, the morphology of sensor device was measured again by SEM and the results were illustrated in Fig. S1. It's obviously found that the hexagonal SnS_2 is prepared on the edge and surface of $Ti_3C_2T_x$. The average thickness and length of SnS_2 nanosheets are about 90.32 nm and 563.12 nm, respectively. The morphology is not changed during the sensor preparation.

Transmission electron microscopy (TEM) and high-resolution TEM (HR-TEM) are conducted to examine the morphological and crystal structures of SnS_2 and $SnS_2/Ti_3C_2T_x$ composites. As displayed in Fig. 5a and b, SnS_2 exhibits a hexagonal structure with an average length of 550 nm. The interplanar spacing of 0.31 nm is assigned to the (100) plane of hexagonal SnS_2 (Fig. 5c). The TEM images of SnS_2 and $Ti_3C_2T_x$ composites are displayed in Fig. 5d and e. Consistent with SEM, hexagonal SnS_2 nanosheets are formed on the edge and surface of $Ti_3C_2T_x$. The HR-TEM image in Fig. 5f shows the heterogeneous interface between SnS_2 and $Ti_3C_2T_x$. The lattice spacings of 0.31 nm and 0.25 nm correspond to the (1 0 0) plane of SnS_2 and the (006) plane of $Ti_3C_2T_x$, respectively. The TEM and SEM images confirm the heterointerfaces are formed in the $SnS_2/Ti_3C_2T_x$ composite.

The chemical states of $SnS_2/Ti_3C_2T_x$ composites are determined by XPS. As shown in Fig. 6a, the high-resolution S 2*p* spectrum of SnS_2 can be fitted with two components at about 161.86 eV and 163.42 eV, attributable to the S $2p_{3/2}$ and S $2p_{1/2}$, respectively. As shown in Fig. 6b, the peaks at about 486.73 eV and 495.17 eV are Sn $3d_{5/2}$ and Sn $3d_{3/2}$, respectively. The survey spectrum shown in Fig. 6c indicates that the $SnS_2/Ti_3C_2T_x$ composite is primarily composed of Sn, Ti, S, and C, consistent with EDS elemental mapping. Fig. 6d presents the Ti 2*p* spectrum of $SnS_2/Ti_3C_2T_x$, showing peaks at about 454.36, 458.91, 461.83, and 464.72 eV. The Ti $2p_{3/2}$ and Ti $2p_{1/2}$ peaks at about 454.36 and 461.83 eV correspond to Ti—C, while those at about 458.91 and 464.72 eV reflect Ti—O. As shown in Fig. 6e and f, the S 2*p* (S $2p_{3/2}$ and S $2p_{1/2}$) and Sn 3*d* (Sn $3d_{5/2}$ and Sn $3d_{3/2}$) peaks at about 161.72 eV/162.93 eV and 486.81 eV/486.83 eV, respectively, confirm the formation of SnS_2 on the surface of $Ti_3C_2T_x$.

3.2. Gas-Sensing properties

Fig. 7a shows the responses of SnS_2, $Ti_3C_2T_x$, and $SnS_2/Ti_3C_2T_x$ composites to 500 ppm NH_3 at RT. The room-temperature response of SnS_2 is about 38.53 %, which is lower than that of $Ti_3C_2T_x$ (51.23 %). When SnS_2 is composited with $Ti_3C_2T_x$, the NH_3-sensing response is enhanced. The sensing response increases as the $Ti_3C_2T_x$ content is

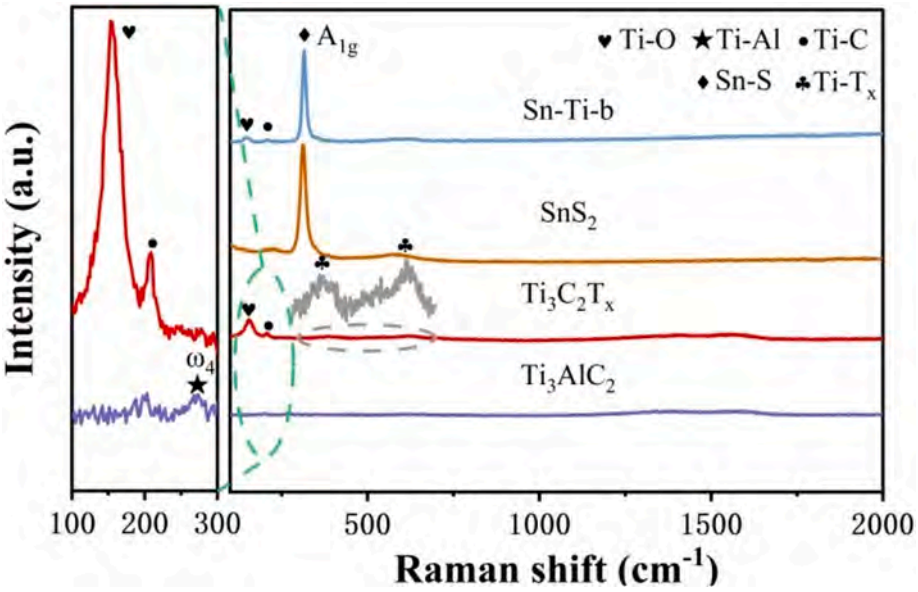

Fig. 3. Raman scattering spectra of Ti_3AlC_2, $Ti_3C_2T_x$, SnS_2 and $SnS_2/Ti_3C_2T_x$ (Sn-Ti-b).

increased from 0 to 0.4 wt% but decreases after that value. The enhancement arises from the uniform SnS_2 nanosheets trapping NH_3 molecules at edge-exposed sites and $Ti_3C_2T_x$ with high conductivity and a large surface area. However, if the content of $Ti_3C_2T_x$ is too high, the adsorption ability degrades due to the reduced availability of active sites for NH_3 adsorption. The results show that the composites with 0.48 wt% $Ti_3C_2T_x$ (Sn-Ti-b) delivers superior NH_3-sensing performance, and therefore, this sample is chosen for further assessment. Fig. 7(b–d) exhibit the dynamic resistance change curves of SnS_2, $Ti_3C_2T_x$, and $SnS_2/Ti_3C_2T_x$ composites to NH_3 at RT. The resistance decreases immediately in NH_3 and then stabilizes, indicative of an n-type semiconducting behavior. After exposure to air, the resistance recovers to the initial state. Fig. 7e presents the relationship of SnS_2, $Ti_3C_2T_x$, and $SnS_2/Ti_3C_2T_x$ composites between the NH_3 concentration and response. The response of Sn-Ti-b sensor is higher than that of SnS_2 and $Ti_3C_2T_x$. The response is enhanced by 0.49864 % at RT for each 1 ppm increase in the NH_3 concentration from 1 to 100 ppm NH_3. In the range of 100–500 ppm NH_3, the response increases slowly. It is only enhanced by 0.04551 % ppm^{-1} at RT. The limit of detection (LOD) is a crucial parameter for gas sensors. The LOD is calculated by Eq. (4) [29–32]:

$$LOD = 3 \times \frac{RMS}{Slope} \tag{4}$$

where *RMS* represents the root-mean-square of noise, and the slope is calculated from the linear response. The LOD of SnS_2/G-b sensor is calculated to be about 143 ppb. Fig. 7f shows the response of Sn-Ti-b sensor to 30–500 ppm NH_3 at RT. With decreasing NH_3 concentration, the response diminishes. The response/recovery times are about 165/1280 s, 56/689 s, 116/521 s, 132/326 s and 169/228 s for 500 ppm, 300 ppm, 100 ppm, 50 ppm, and 30 ppm NH_3, respectively (Fig. 7g). Good selectivity is also important to practical applications. The acetone, ethanol, H_2S, H_2, methanol, SO_2 and trimethylamine (TMA) are the common harmful gas. Especially, the TMA is also a marker of food spoilage. Hence, these gases are selected as the test gas. As displayed in Fig. 7h, the response to 100 ppm NH_3 is about 61.23 %, which is much higher than that to acetone (2.36 %), ethanol (3.12 %), H_2S (1.36 %), H_2 (1.12 %), methanol (0.36 %), SO_2 (5.36 %) and TMA (23.37 %), indicating that SnS_2 and $Ti_3C_2T_x$ composites in this work show the excellent selectivity to NH_3. To reveal the selectivity mechanism of SnS_2 and $Ti_3C_2T_x$ composites, the adsorption energy of SnS_2 toward NH_3, acetone, ethanol, H_2S, H_2, methanol and SO_2 was calculated and the results were illustrated in Fig. S2. The adsorption energy of SnS_2 toward NH_3 is much more negative that of SnS_2 toward other gases, indicating the stronger adsorption ability to NH_3 molecular. Hence, fabrication of SnS_2 and $Ti_3C_2T_x$ composites show the excellent selectivity to NH_3 gas molecular. Fig. 7i shows the resistance changes of Sn-Ti-b to 100 ppm NH_3 in five successive cycles at RT. Although the resistance baseline drifts slightly after five cycles, the responses are basically similar, implying good repeatability. The antioxidant properties of $Ti_3C_2T_x$ is evaluated by recording the baseline resistance of $Ti_3C_2T_x$ and $SnS_2/Ti_3C_2T_x$ composites in the long-term stability tests and the results are displayed in Fig. S3. The relative standard deviation (RSD) of resistance of $Ti_3C_2T_x$ and $SnS_2/Ti_3C_2T_x$ composites are about 61.64 % and 30.49 %, respectively. Additionally, after 10 days, the resistance of $Ti_3C_2T_x$ was increased by 289.4 % While, the resistance of $SnS_2/Ti_3C_2T_x$ composites is not almost changed. Hence, fabrication of SnS_2 and $Ti_3C_2T_x$ composites could enhance the antioxidant properties of $Ti_3C_2T_x$. In addition, the long-term stability of Sn-Ti-b toward 100 ppm NH_3 at RT is displayed in Fig. S4. The response exhibits relatively slight fluctuations, showing a decrease only by 13.45 % after 15 days, behaving the excellent long-term stability.

The sensing response of Sn-Ti-b at different temperatures and environmental humidity (RH) is investigated. As shown in Fig. 8a, with increasing temperature, the sensor exhibits a downward trend. At a high temperature, NH_3 molecules move faster and desorb before they have time to participate in reaction, thus giving rise to a poor response [29–32]. Fig. 8b shows the response of Sn-Ti-b to 100 ppm NH_3 at different RH, revealing a decreasing trend as the RH goes up from 35 % to 87 %. At high humidity, H_2O molecules adsorb easily from the air onto the sensing surface. The hydroxyl group of H_2O may be dissociated and serves as an electron donor to transfer electrons into the conduction band and reduce resistance. At same time, the adsorbed H_2O molecules on the surface inhibit the adsorption of NH_3 to reduce the response at RT [30–33]. In addition, the comparison of NH_3-sensing performance of $SnS_2/Ti_3C_2T_x$ composites in this work with other previous work is presented in Table S1 [11,12,34–39]. The pure $Ti_3C_2T_x$ and V_2CT_x show the poor room-temperature NH_3-sensing response [34–36]. The SnS_2 show the excellent NH_3-sensing response. While, the working temperature is high [11,12]. For the SnO_2/SnS_2 [37], $Ti_3C_2T_x/TiO_2$ [38] and PANI/$Ti_3C_2T_x$ [39] composites, the working temperature is RT. While the response is lower. Hence, fabrication of SnS_2 and $Ti_3C_2T_x$ composites in this work could realize the excellent NH_3-sensing response at RT.

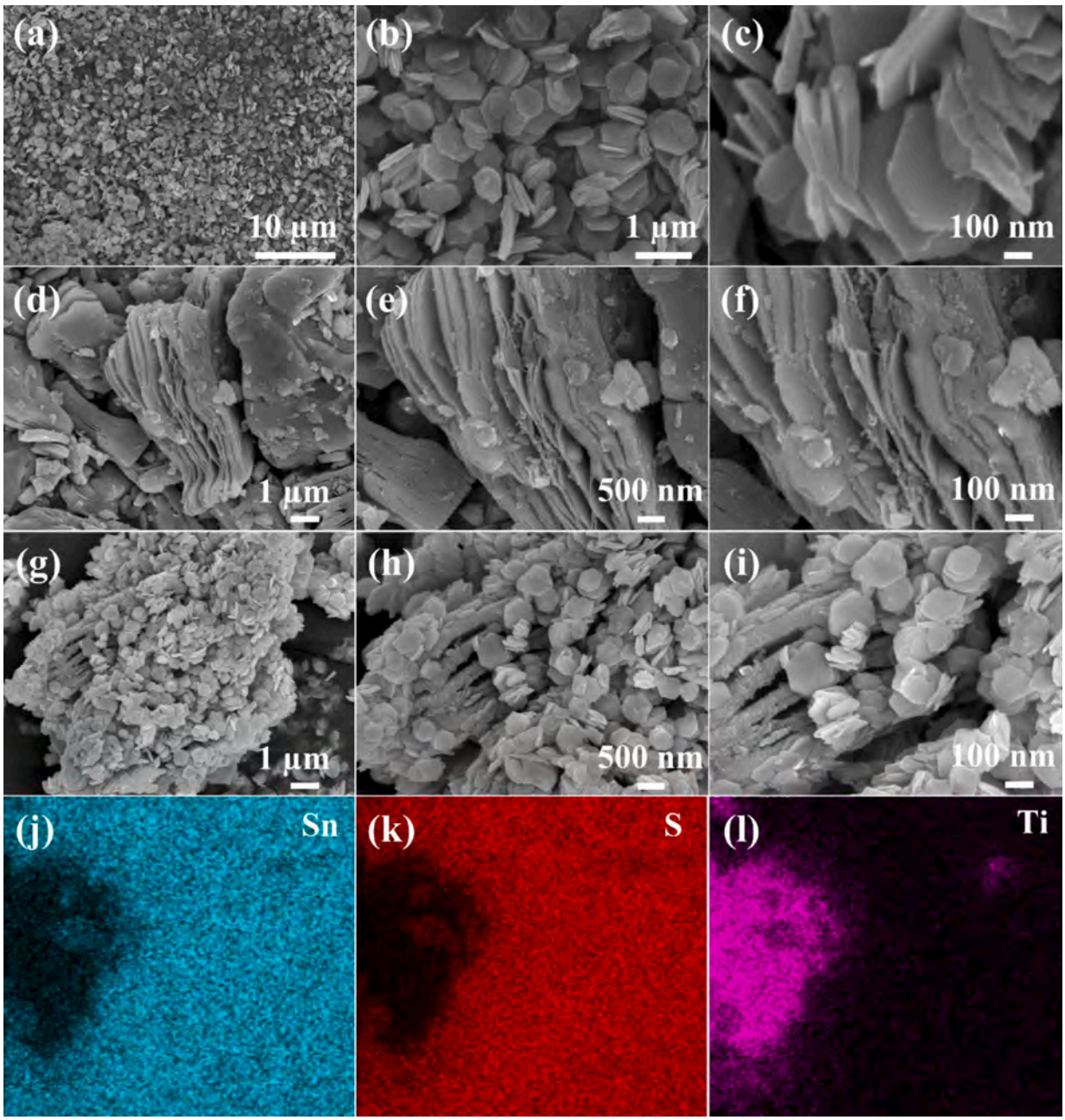

Fig. 4. SEM images of (a-c) SnS_2, (d-f) $Ti_3C_2T_x$, (g-i) $SnS_2/Ti_3C_2T_x$ composites (Sn-Ti-b) and (j-l) EDS elemental maps of the SnS_2 and $Ti_3C_2T_x$ composite (Sn-Ti-b).

3.3. Gas sensing mechanism

During gas sensing, chemical adsorption, oxidation, and desorption occur at the interface between NH_3 and $SnS_2/Ti_3C_2T_x$ composites. In air, the oxygen is adsorbed on the surface of composites and captures electrons to form the chemisorbed oxygen ions (O_2^-). In NH_3, the NH_3 molecular would react with adsorbed O_2^- ions to release electrons to the composite and thus the resistance is reduced (Eq. (5)–(8)). The adsorbates on the $SnS_2/Ti_3C_2T_x$ composite have been determined previously by *in situ* DRIFTS [28]. As shown in Fig. S5, the black curve shows the spectra of $SnS_2/Ti_3C_2T_x$ composites in air, and the other curves show the spectra of $SnS_2/Ti_3C_2T_x$ composites in NH_3. The peaks at 1,070 cm^{-1} and 1,563 cm^{-1} are related to N—H bonds coupled to Lewis acid sites, while those at 1,506 cm^{-1}, 1,539 cm^{-1}, and 1,693 cm^{-1} are associated with NH_4^+ chemisorbed at Brønsted acid sites. The Lewis and Brønsted acid sites have strong adsorption ability toward alkaline NH_3. The strong peaks at 1,624 cm^{-1} and 1,693 cm^{-1} correspond to adsorbed NO_2, indicating that NO_2 is generated in the gas-sensing process [28].

$$O_2(gas) \rightarrow O_2(ads) \quad (5)$$

$$O_2(ads) + e^- \rightarrow O_2^-(ads) \quad (6)$$

$$4NH_3(gas) + 5O_2^-(ads) \rightarrow 4NO + 6H_2O + 5e^- \quad (7)$$

$$2NO(ads) + O_2(gas) \rightarrow 2NO_2 \quad (8)$$

Fig. 9 shows the adsorption energies of SnS_2, $Ti_3C_2T_x$, and $SnS_2/Ti_3C_2T_x$ heterojunction toward NH_3 molecular. The adsorption energies of SnS_2 and $Ti_3C_2T_x$ heterojunctions for NH_3 are much more negative than those of SnS_2 and $Ti_3C_2T_x$. It indicates that the composite has enhanced adsorption ability for NH_3. The adsorbed oxygen captures electrons from n-type SnS_2 to form chemisorbed oxygen ions (O_2^-), and the NH_3 molecular reacts with O_2^- to release electrons to the composite,

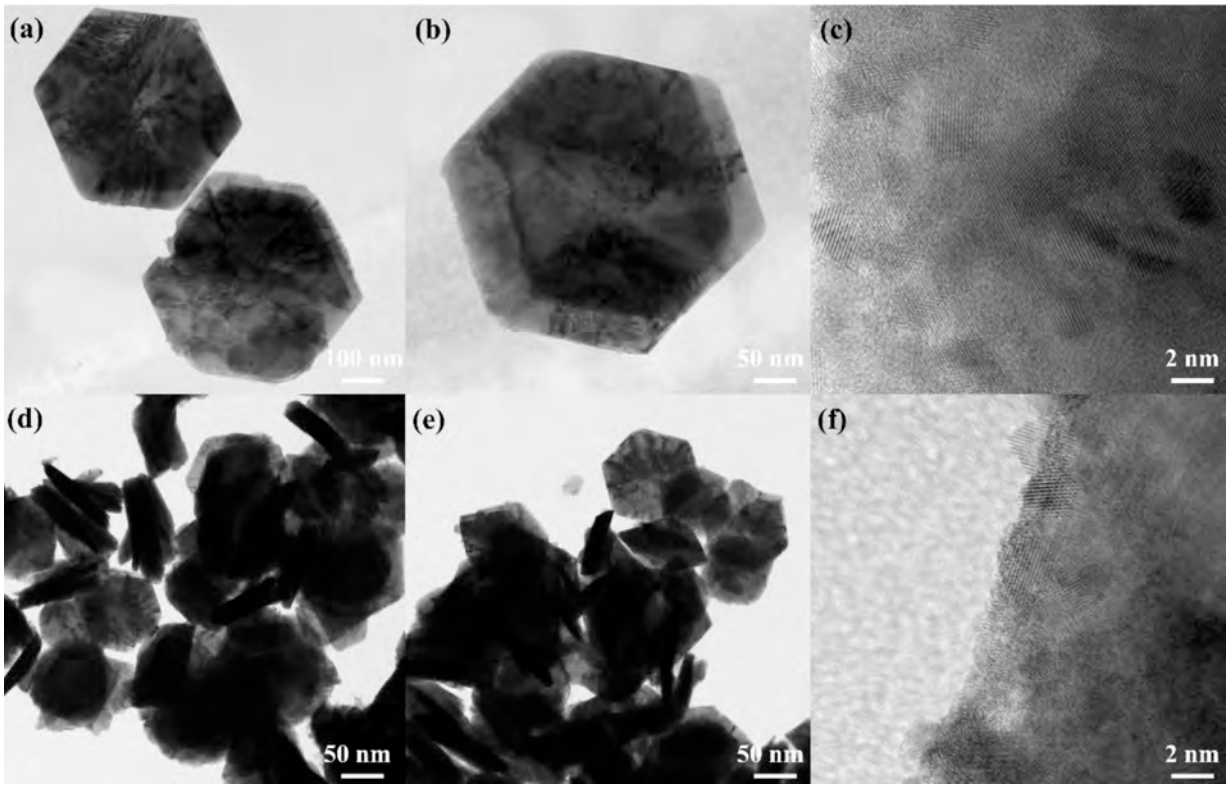

Fig. 5. TEM images of (a-c) SnS_2 and (d-f) $SnS_2/Ti_3C_2T_x$ composite (Sn-Ti-b).

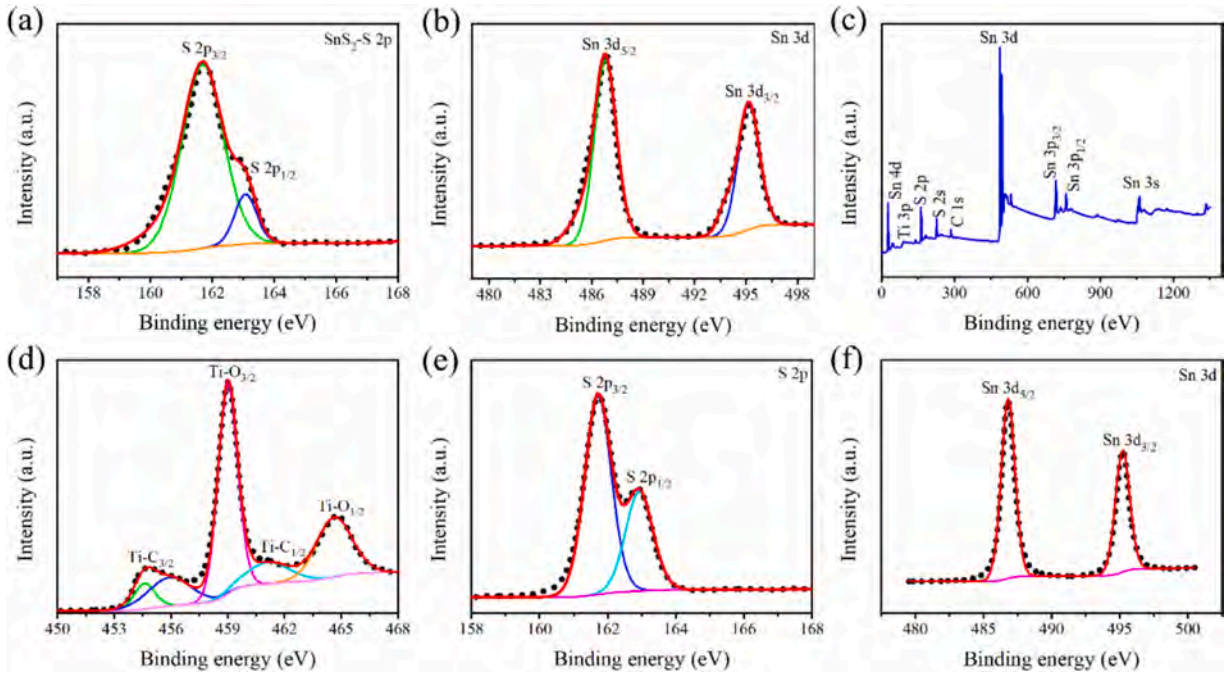

Fig. 6. (a) XPS S 2*p* and (b) Sn 3*d* spectra of SnS_2; (c) Survey, (d) Ti *s*, (e) S 2*p*, (f) and Sn 3*d* spectra of SnS_2/graphene (SnS_2/G-b).

reducing the resistance [28–30]. In addition, the Ultraviolet–visible (UV–vis) absorption spectra of SnS_2, $Ti_3C_2T_x$ and composites are measured and the results are shown in Fig. S6. The band gap of SnS_2, $Ti_3C_2T_x$ and composites are about 2.07 eV, 1.58 eV and 1.35 eV, respectively. Hence, fabrication of SnS_2 and $Ti_3C_2T_x$ composites could reduce the band gap and thus enhance the conductivity.

The interaction between SnS_2 and $Ti_3C_2T_x$ MXene could be explained by the structural interaction and heterojunction interaction. According to the results of SEM, the $Ti_3C_2T_x$ show the accordion-like multilayer nanosheet structure. It has the larger surface area and high carrier mobility. The SnS_2 has the strong adsorption ability for NH_3 molecular. The uniform hexagonal structure and edge-exposed SnS_2 nanosheets deposited on the conductive $Ti_3C_2T_x$ have a large surface area to promote the adsorption of NH_3 molecules. At the same time, SnS_2 prevents

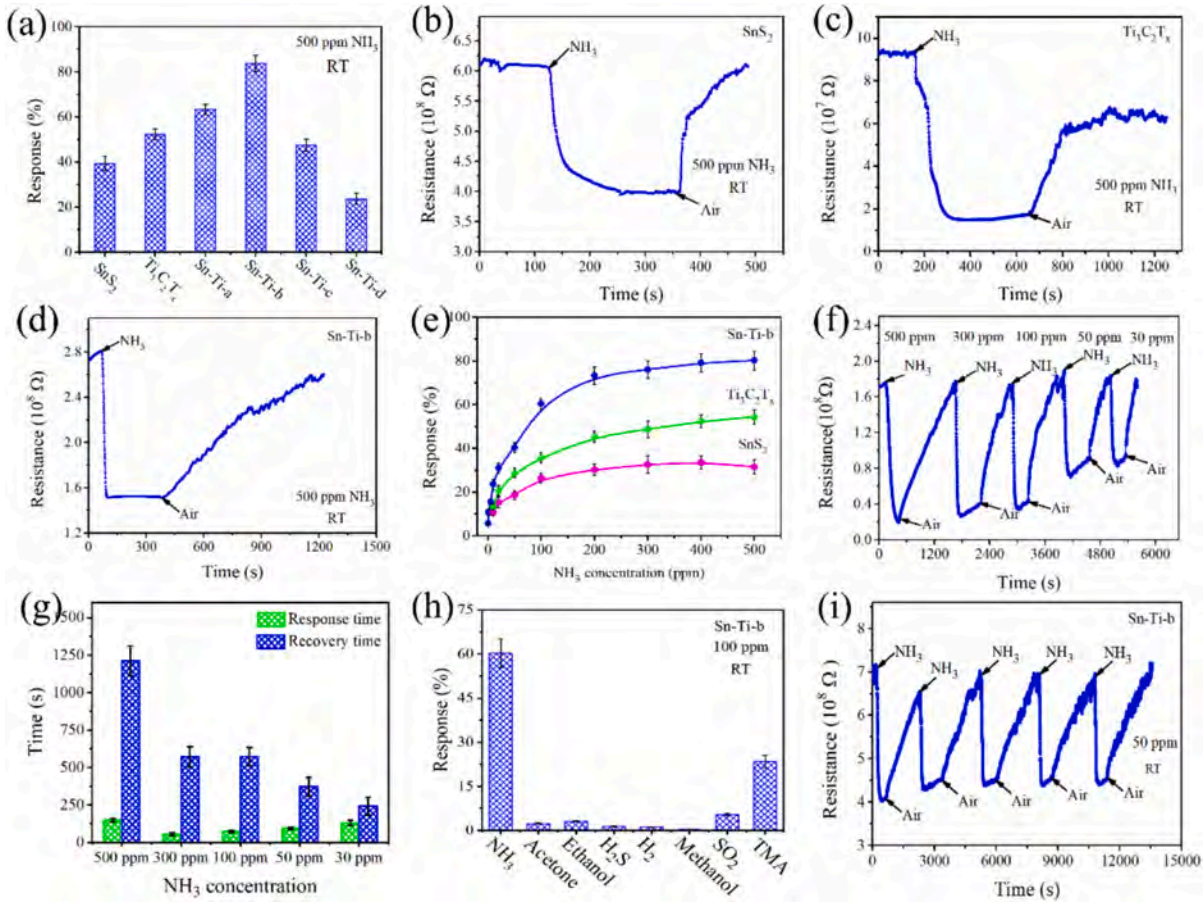

Fig. 7. (a) Response of SnS_2, $Ti_3C_2T_x$ and $SnS_2/Ti_3C_2T_x$ composites; Real-time resistance variations of (b) SnS_2, (c) $Ti_3C_2T_x$, and (d) Sn-Ti-b to 500 ppm NH_3 at RT; (e) Response of Sn-Ti-b to 1–500 ppm NH_3 at RT; (f) Response curve of Sn-Ti-b to 30–500 ppm NH_3 at RT; (g) Response and recovery time of Sn-Ti-b to 30–500 ppm NH_3 at RT; (h) The selectivity of Sn-Ti-b to 100 ppm NH_3 at RT; (i) Five cycle repeatability of Sn-Ti-b to 50 ppm NH_3 at RT.

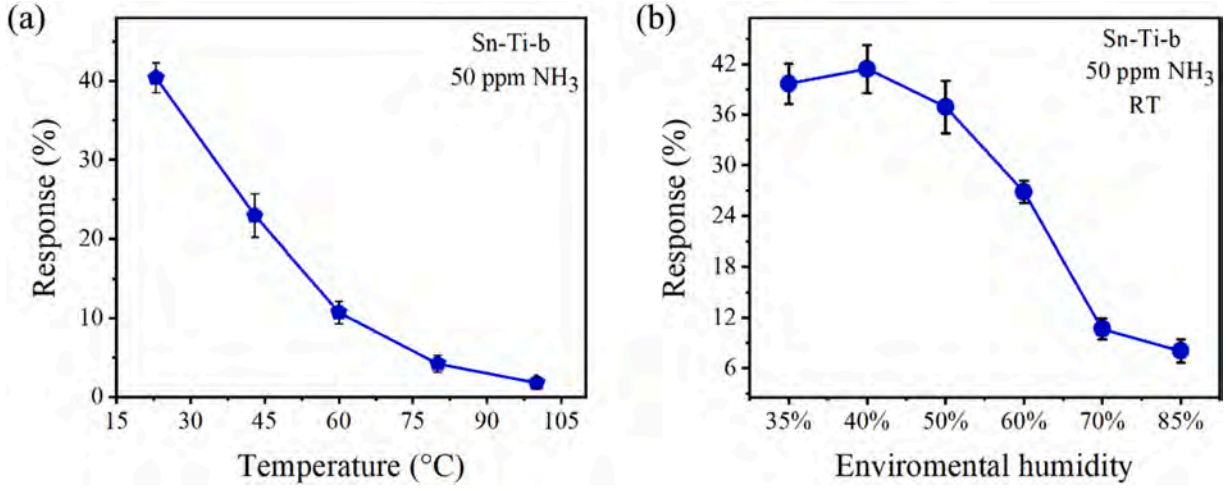

Fig. 8. Response of Sn-Ti-b to 50 ppm NH_3: (a) Temperature and (b) Relative humidity.

oxidation-induced degradation of $Ti_3C_2T_x$ to improve the stability.

To reveal the effects of the heterojunction on the NH_3-sensing performance, the work functions is calculated. As shown in Fig. 10, the work function of SnS_2 is smaller than that of $Ti_3C_2T_x$ [28]. When SnS_2 is in contact with $Ti_3C_2T_x$, electrons are transferred from SnS_2 to $Ti_3C_2T_x$ to establish an equilibrium Fermi level. Electron injection gives rise to band bending in both materials and formation of Schottky barriers at interface. Upon exposure to NH_3, the reaction with adsorbed oxygen releases electrons back to the sensing materials to increase the electron density, reduce the Schottky barrier height, and promote electron transfer at interface. As a result, the electrical conductivity increases and the NH_3-sensing response is enhanced.

Finally, the density of states (DOS) and partial density of states (PDOS) of SnS_2, $Ti_3C_2T_x$, and $SnS_2/Ti_3C_2T_x$ composites are calculated and displayed in Fig. 11. As shown in Fig. 11a and b, SnS_2 has a larger bandgap (E_g = 1.734 eV). The conduction band bottom (CBB) and

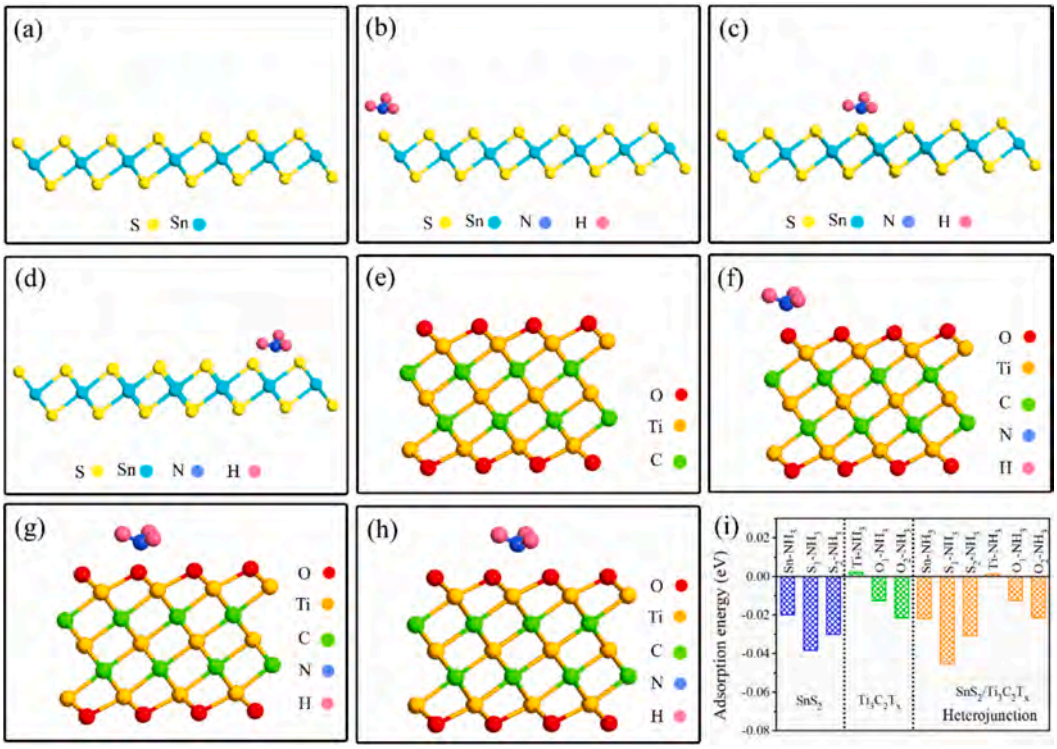

Fig. 9. Side views of (a) SnS_2, (b-d) SnS_2 adsorbing NH_3, (e) $Ti_3C_2T_x$, (f-h) $Ti_3C_2T_x$ adsorbing NH_3, and (i) Adsorption energies of SnS_2, $Ti_3C_2T_x$ and composites for NH_3 molecular.

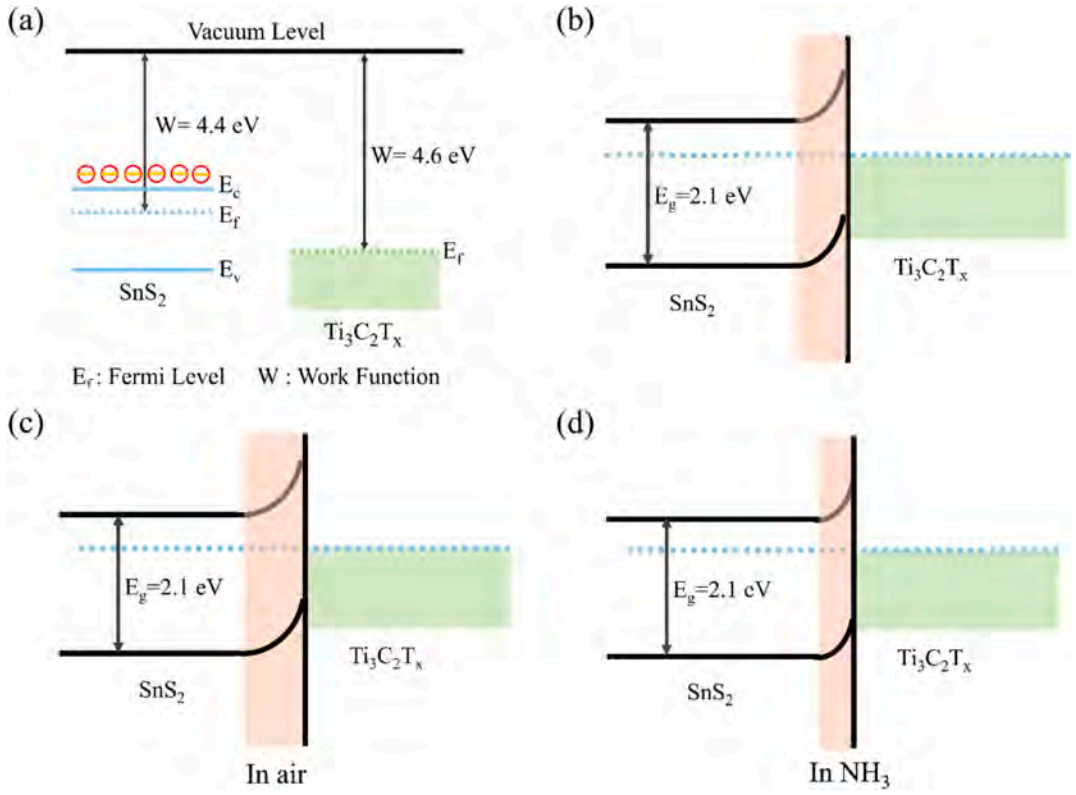

Fig. 10. (a) Work functions of SnS_2 and $Ti_3C_2T_x$; Energy band diagrams of the heterojunction in (b) Vacuum, (c) Air, and (d) NH_3.

valence band top (VBT) are mainly composited with Sn *s* and S *p* states, respectively. At RT, electrons are harder to transfer from VBT to CBB, resulting in poor conductivity. As for $Ti_3C_2T_x$, the CBB and VBT overlap at the Fermi level, thus showing metallic properties. The bandgap of $SnS_2/Ti_3C_2T_x$ composites decreases to 0.12 eV with the CBB and VBT being mainly the Ti *d* and S *s* states, respectively. At RT, electrons are

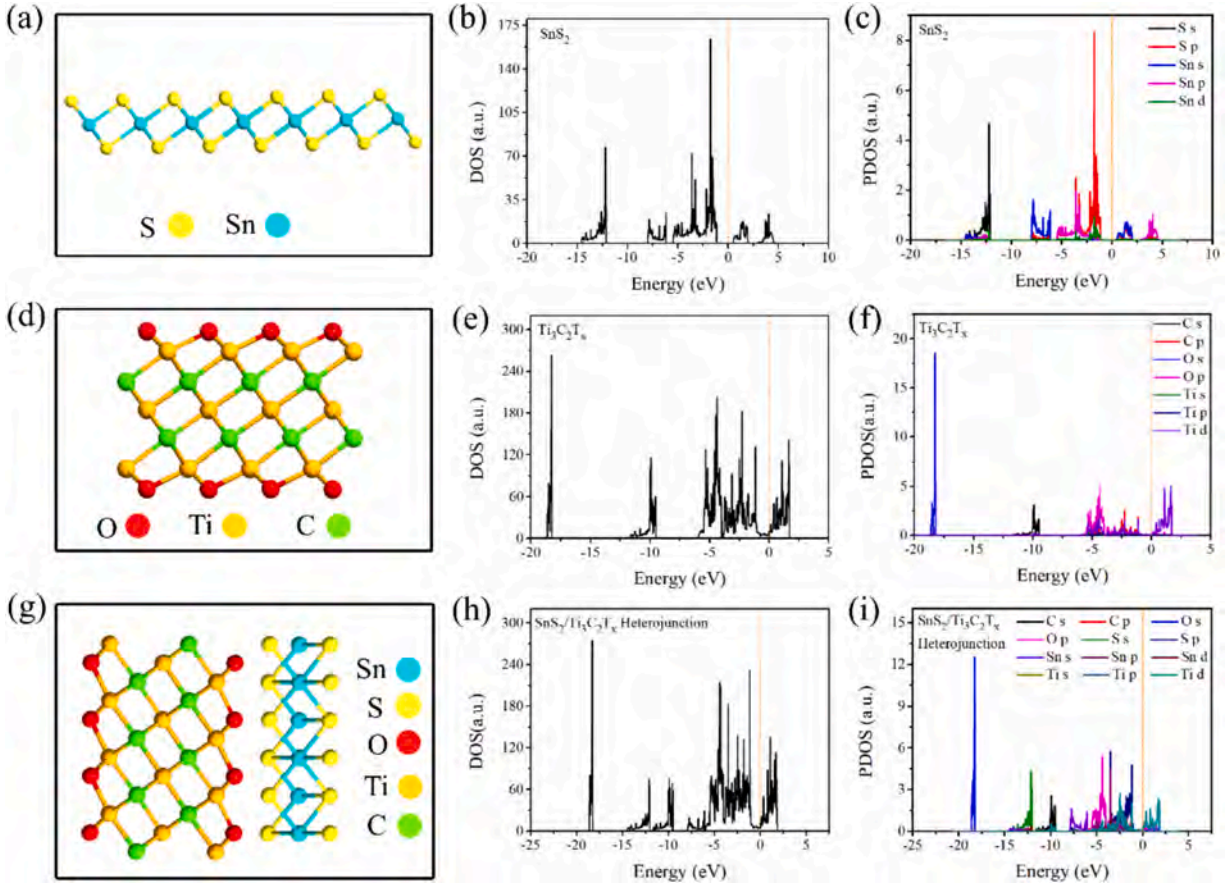

Fig. 11. Atomic structure, DOS, and PDOS of (a-c) SnS_2, (d-f) $Ti_3C_2T_x$, and (g-i) $SnS_2/Ti_3C_2T_x$ heterojunction.

transferred from VBT to CBB easily, thereby increasing the conductivity and providing electron exchange between SnS_2 and $Ti_3C_2T_x$. Therefore, the heterojunction improves charge transfer and ultimately the sensing properties.

4. Conclusion

The NH_3 gas sensing performance of SnS_2 and $Ti_3C_2T_x$ composites at RT is studied. Surface functionalization of $Ti_3C_2T_x$ with SnS_2 enhances the adsorption capacity and charge transfer ability for NH_3 to improve the sensing properties. Compared with SnS_2 and $Ti_3C_2T_x$, the response of $SnS_2/Ti_3C_2T_x$ composites to 50 ppm NH_3 at RT is enhanced by 34.5 % and 52.6 %, respectively. Additionally, the sensor exhibits better selectivity, long-term stability, and fast response and recovery rates. DFT calculations reveal that the adsorption capability of SnS_2 to NH_3 is much stronger than that of $Ti_3C_2T_x$, indicating that introduction of SnS_2 on the surface of $Ti_3C_2T_x$ could provide optimal active sites for adsorption of NH_3. In addition, based on the DFT calculation, the bandgap of SnS_2 and $Ti_3C_2T_x$ heterojunction is about 0.12 eV, consequently boosting electron exchange at interface and improving the sensing response. The experimental and theoretical findings confirm that the SnS_2 and $Ti_3C_2T_x$ composite is an ideal candidate for high-sensitivity room-temperature NH_3 gas sensors.

CRediT authorship contribution statement

Lizhai Zhang: Writing – review & editing, Writing – original draft, Funding acquisition, Formal analysis. **Jiayuan Xu:** Validation, Software, Methodology. **Xinyu Lei:** Software, Methodology, Formal analysis. **Henghui Sun:** Software, Project administration, Formal analysis. **Taotao Ai:** Software, Funding acquisition, Formal analysis. **Fei Ma:** Methodology, Investigation, Conceptualization. **Paul K Chu:** Writing – review & editing, Resources, Methodology.

Declaration of competing interest

The authors declare that they have no known competing financial interests or personal relationships that could have appeared to influence the work reported in this paper.

Acknowledgments

This work was jointly supported by the Natural Science Foundation of Shaanxi Province (2023-JC-QN-0476), Shaanxi University of Technology Research Grant (no. SLGRCQD2207), Scientific research project of Shaanxi Provincial Education Department (no.23JK0375), Science and technology program for overseas students of Shaanxi province (2023016), and City University of Hong Kong Donation Research Grants (DON-RMG no.9229021 and 9220061).

Appendix A. Supplementary data

Supplementary data to this article can be found online at https://doi.org/10.1016/j.apsusc.2025.164190.

Data availability

No data was used for the research described in the article.

References

[1] S. Kim, Y. Kim, J. Kim, S.J. Kim, T. Kim, J. Sim, S.E. Jun, J. Lim, T.H. Eom, H.S. Lee, G.H. Lee, B.H. Hong, M.H. Oh, Y.S. Huh, H.W. Jang, Highly selective ammonia detection in NiO-functionalized graphene micropatterns for beef quality monitoring, Adv. Funct. Mater. 34 (2024) 2407885.

[2] L.X. Yan, L.J. Chen, X. Zhao, X.P. Yan, pH switchable nanoplatform for in vivo persistent luminescence imaging and precise photothermal therapy of bacterial infection, Adv. Funct. Mater. 30 (2020) 1909042.

[3] G.J.E. Nychas, D. Dourou, P. Skandamis, K. Koutsoumanis, J. Baranyi, J. Sofos, Effect of microbial cell-free meat extract on the growth of spoilage bacteria, J. Appl. Microbiol. 107 (2009) 1819–1829.

[4] F. Jiao, B.J. Xu, Electrochemical ammonia synthesis and ammonia fuel cells, Adv. Mater. 31 (2019) 1805173.

[5] H.W. Chen, Y.T. Chen, H. Zhang, D.W. Zhang, P. Zhou, J. Huang, Suspended SnS_2 layers by light assistance for ultrasensitive ammonia detection at room temperature, Adv. Funct. Mater. 28 (2018) 1801035.

[6] M.P. Shaver, M.D. Fryzuk, Activation of molecular nitrogen: coordination, cleavage and functionalization of N_2 mediated by metal complexes, Adv. Synth. Catal. 345 (2003) 1061–1076.

[7] Y.H. Kim, J.S. Park, Y.R. Choi, S.Y. Park, S.Y. Lee, W. Sohn, Y.S. Shim, J.H. Lee, C. R. Park, Y.S. Choi, B.H. Hong, J.H. Lee, W.H. Lee, D. Lee, H.W. Jang, Chemically fluorinated graphene oxide for room temperature ammonia detection at ppb levels, J. Mater. Chem. A 5 (2017) 19116–19125.

[8] Z.Y. Qin, K. Xu, H.C. Yue, H. Wang, J. Zhang, C. Ouyang, C.S. Xie, D.W. Zeng, Enhanced room-temperature NH_3 gas sensing by 2D SnS_2 with sulfur vacancies synthesized by chemical exfoliation, Sens. Actuators B Chem. 262 (2018) 771–779.

[9] R.K. Mishra, H.J. Choi, J.W. Ryu, G.J. Choi, V. Kumar, P. Kumar, J. Singh, S. Kumar, J.S. Gwag, Recent progress in gas sensing based on 2D SnS_2 and its heterostructure platforms: a review, Sens. Actuators B Chem. 365 (2024) 114860.

[10] Z.J. Lei, M.H. Lin, Y. Zhou, C.F. Huang, J.Y. Chen, H.H. Mao, J.X. Cao, X. P. OuYang, Glucose-modulated defect-enriched S_v-SnS_2 sensor for rapid detection of NH_3 at room temperature, J. Alloy. Compd. 1026 (2025) 180379.

[11] Y. Xiong, W.W. Xu, D.G. Ding, W.B. Lu, L. Zhu, Z.Y. Zhu, Y. Wang, Q.Z. Xue, Ultra-sensitive NH_3 sensor based on flower-shaped SnS_2 nanostructures with sub-ppm detection ability, J. Hazard. Mater. 341 (2018) 159–167.

[12] Q.X. Zhang, S.Y. Ma, G.J. Yang, R. Zhang, X.T. Wang, Q. Chen, L. Ma, S.T. Pei, K. M. Zhu, W.Q. Wang, Y. Tie, 3D SnS_2 hierarchical micro-flowers synthesized by $ZnSn(OH)_6$ for ultra-sensitive NH_3 sensor, Mater. Lett. 236 (2019) 600–603.

[13] R.M. Zhao, T.X. Wang, M.Y. Zhao, C.X. Xia, X. Zhao, Y.P. An, X.Q. Dai, A theoretical simulation of small-molecules sensing on an S-vacancy SnS_2 monolayer, Phys. Chem. Chem. Phys. 19 (2017) 10470–10480.

[14] Z.J. Liao, Z.Y. Yuan, Y. Yu, R.Z. Zhang, H.M. Zhu, H.L. Gao, F.L. Meng, Ppb-level ammonia sensors based on SnS_2/rGO nanohybrid operating at room temperature, IEEE Trans. Nanotechnol. 22 (2023) 722–731.

[15] C.Y. Liang, P. Li, S.G. Yu, Q. Jing, Y.H. Niu, Design and mechanism study of fast response MoS_2/SnS_2 heterojunction ammonia sensor for gas detection in chicken coops, J. Alloy. Compd. 1022 (2024) 179906.

[16] T.T. Wang, B.S. Xing, C.Y. Guo, J.Y. Hao, Y. Wang, L.H. Huo, X.L. Cheng, Y.M. Xu, Recent advances of emerging tin disulfide for room temperature gas sensing, Rare Met. 42 (2023) 3897–3913.

[17] L.Z. Zhang, J.Y. Xu, X.Y. Lei, H.H. Sun, T.T. Ai, F. Ma, P.K. Chu, Edge-enriched SnS_2 nanosheets on graphene for chemiresistive room temperature NH_3 sensors, Sens. Actuators B Chem. 433 (2025) 137565.

[18] L.T. Nhiem, J.B. Mao, Q.T.H. Ta, S. Seo, Highly selective ethanol gas sensor based on CdS/$Ti_3C_2T_x$ MXene composites, Nanoscale Adv. 5 (2025) 1452–1463.

[19] M.N. Tran, A. Skorynina, A. Addad, A. Fade, K. Ben Tayeb, L. Karmazin, L. Thomas, M. Gorda, Y. Wisse, O. Vovk, A.Y. Khodakov, B. Grandidier, V. Ordomsky, Electricity-driven selectivity in the photocatalytic oxidation of methane to carbon monoxide with liquid gallium-semiconductor composite, Appl. Catal. B Environ. 363 (2025) 124834.

[20] K.S. Ranjith, S. Sonwal, A. Mohammadi, G.S.R. Raju, Y.S. Huh, Y.K. Han, Engineering a surface functionalized Pt@SnS_2/$Ti_3C_2T_x$ MXene sensor with humidity tolerance and high sensitivity at room temperature for NH_3 detection, J. Mater. Chem. A 13 (2025) 2950–2964.

[21] K.X. Cheng, X. Tian, S.R. Yuan, Q.Y. Feng, Y.D. Wang, Research progress on ammonia sensors based on $Ti_3C_2T_x$ MXene at room temperature: a review, Sensors 24 (2024) 4465.

[22] H.F. Zhang, J.Y. Xuan, Q. Zhang, M.L. Sun, F.C. Jia, X.M. Wang, G.C. Yin, S.Y. Lu, Strategies and challenges for enhancing performance of MXene-based gas sensors: a review, Rare Met. 41 (2022) 3976–3999.

[23] Q.F. Li, M.H. Xu, X.N. Wei, Z.C. Chen, Room temperature ammonia sensors with enhanced sensitivity based on CuO/$Ti_3C_2T_x$/graphene composites, IEEE Sens. J. 25 (2025) 7991–7999.

[24] S. Gasso, J. Carrier, D. Radu, C.Y. Lai, Novel gas sensing approach: ReS_2/$Ti_3C_2T_x$ heterostructures for NH_3 detection in humid environments, ACS Sens. 9 (2024) 4788–4802.

[25] G. Kresse, J. Furthmüller, Efficient iterative schemes for ab initio total-energy calculations using a plane-wave basis set, Phys. Rev. B 54 (1996) 11169–11186.

[26] G. Kresse, J. Hafner, Ab initio molecular dynamics for open-shell transition metals, Phys. Rev. B 48 (1993) 13115–13118.

[27] G. Kresse, D. Joubert, From ultrasoft pseudopotentials to the projector augmented-wave method, Phys. Rev. B 59 (1999) 1758–1775.

[28] T.T. He, S.P. Sun, B.Y. Huang, X.G. Li, MXene/SnS_2 heterojunction for detecting sub-ppm NH_3 at room temperature, ACS Appl. Mater. Interfaces 15 (2023) 4194–4207.

[29] H. Long, A. Harley-Trochimczyk, T. Pham, Z.R. Tang, T.L. Shi, A. Zettl, C. Carraro, M.A. Worsley, R. Maboudian, High surface area MoS_2/graphene hybrid aerogel for ultrasensitive NO_2 detection, Adv. Funct. Mater. 26 (2020) 5158–5165.

[30] L.T. Duy, D.J. Kim, T.Q. Trung, V.Q. Dang, B.Y. Kim, H.K. Moon, N.E. Lee, High performance three-dimensional chemical sensor platform using reduced graphene oxide formed on high aspect-ratio micro-pillars, Adv. Funct. Mater. 25 (2015) 883–890.

[31] F. Liu, J.B. Zhao, C.Z. Chen, H. Zhou, N. Xiang, Z.D. Jin, L. Liu, S.Q. Li, J.R. Liu, L. L. Wu, Dual enhancement in response and anti-humidity properties of a triethylamine sensor based on trimethoxypropylsilane self-assembled functionalized In_2O_3, Sens. Actuators B Chem. 417 (2024) 136120.

[32] L.Z. Zhang, J.Y. Xu, X.L. Yang, X.Y. Lei, H.H. Sun, Y.H. Huang, H.B. Lu, T.T. Ai, F. Ma, P.K. Chu, Edge-enriched CeO_2/MoS_2 heterostructure with coupled interface for enabling selective room-temperature NO_2 detection, Sens. Actuators B Chem. 419 (2024) 136443.

[33] B. Das, S. Behera, B. Satpati, R. Ghosh, Layered SnS_2/porous nickel foil based Schottky junction: an excellent ammonia sensor at room temperature, J. Hazard. Mater. 428 (2022) 128252.

[34] S.J. Kim, H.J. Koh, C.E. Ren, O. Kwon, K. Maleski, S.Y. Cho, B. Anasori, C.K. Kim, Y. K. Choi, J. Kim, Y. Gogotsi, H.T. Jung, Metallic $Ti_3C_2T_x$ MXene gas sensors with ultrahigh signal-to-noise ratio, ACS Nano 12 (2018) 986–993.

[35] M. Wu, M. He, Q. Hu, Q. Wu, G. Sun, L. Xie, Z. Zhang, Z. Zhu, A. Zhou, Ti_3C_2 MXene based sensors with high selectivity for NH_3 detection at room-temperature, ACS Sens. 4 (2019) 2763–2770.

[36] E. Lee, A. VahidMohammadi, Y.S. Yoon, M. Beidaghi, D.J. Kim, Two-dimensional vanadium carbide MXene for gas sensors with ultrahigh sensitivity toward nonpolar gases, ACS Sens. 4 (2019) 1603–1611.

[37] K. Xu, N. Li, D. Zeng, S.Q. Tian, S.S. Zhang, D. Hu, C. Xie, Interface-bonds determined gas sensing of SnO_2-SnS_2 hybrids to ammonia at room temperature, ACS Appl. Mater. Interface 7 (2015) 11359–11368.

[38] H. Tai, Z. Duan, Z. He, X. Li, J. Xu, B. Liu, Y. Jiang, Enhanced ammonia response of $Ti_3C_2T_x$ nanosheets supported by TiO_2 nanoparticles at room temperature, Sens. Actuators B 298 (2019) 126874.

[39] X. Li, J. Xu, Y. Jiang, Z. He, B. Liu, H. Xie, H. Li, Z. Li, Y. Wang, H. Tai, Toward agricultural ammonia volatilization monitoring: a flexible polyaniline/$Ti_3C_2T_x$ hybrid sensitive films based gas sensor, Sens. Actuators B 316 (2020) 128144.

Supporting information

Highly Selective Ammonia Detection in SnS_2 nanosheets Functionalized $Ti_3C_2T_x$

Lizhai Zhang[a,b,c,e], Jiayuan Xu[d], Xinyu Lei[a], Henghui Sun[a], Taotao Ai[a*], Fei Ma [b,e], Paul K Chu [c*]*

[a] School of Materials Science and Engineering, Shaanxi University of Technology, Hanzhong 723001, Shaanxi, China

[b] State Key Laboratory for Mechanical Behavior of Materials, Xi'an Jiaotong University, Xi'an 710049, Shaanxi, China

[c] Department of Physics, Department of Materials Science and Engineering, and Department of Biomedical Engineering, City University of Hong Kong, Tat Chee Avenue, Kowloon, Hong Kong, China

[d] Shaanxi Engineering and Technology Research Center for Industrialization of Natural Active Products, Shaanxi University of Technology, Hanzhong, Shaanxi 723001, China

[e] College of Physics and Information Technology, Shaanxi Normal University, Xi'an 710062, Shaanxi, China

*Address correspondence to: zhanglizhai0512@snut.edu.cn (L. Z. Zhang);

aitaotao0116@126.com (T. T. Ai); paul.chu@cityu.edu.hk (P. K. Chu)

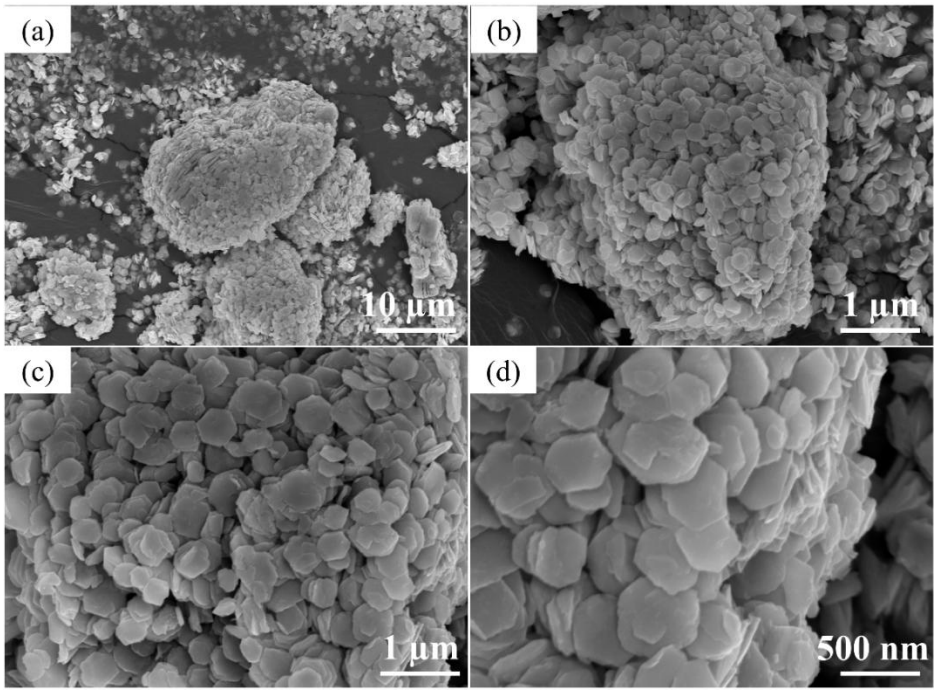

Fig. S1. The morphology of $SnS_2/Ti_3C_2T_x$ composites in the sensor device.

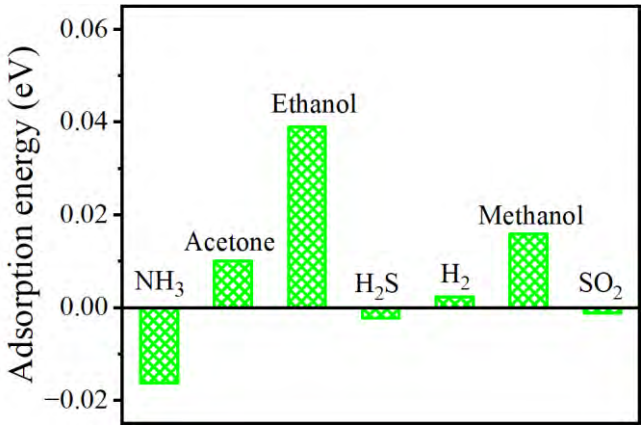

Fig. S2. The adsorption energy of SnS_2 toward NH_3, acetone, ethanol, H_2S, H_2, methanol and SO_2 molecular.

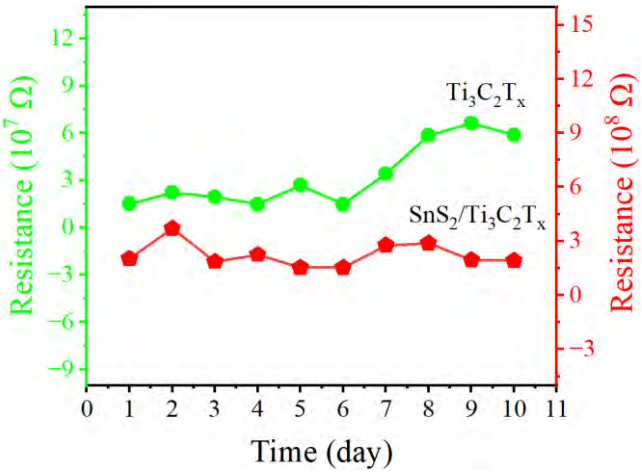

Fig. S3. The baseline resistance of $Ti_3C_2T_x$ and $SnS_2/Ti_3C_2T_x$ composites in 10 days.

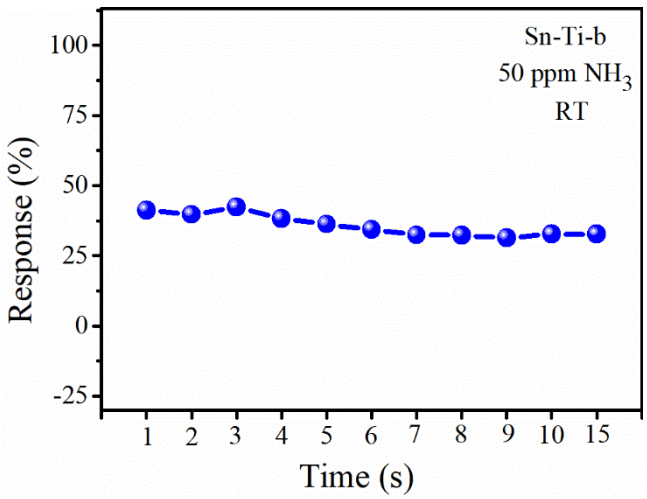

Fig. S4. Long-term stability of the SnS_2 and $Ti_3C_2T_x$ composites toward 50 ppm NH_3 at RT.

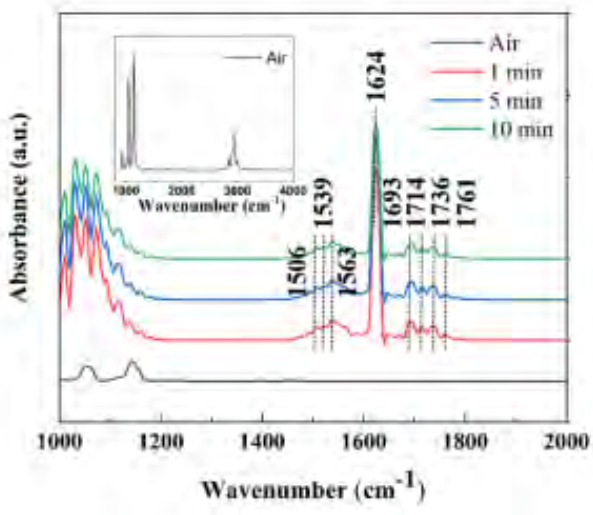

Fig. S5. In situ DRIFT spectra of the SnS_2 and $Ti_3C_2T_x$ composites in air and NH_3 [25].

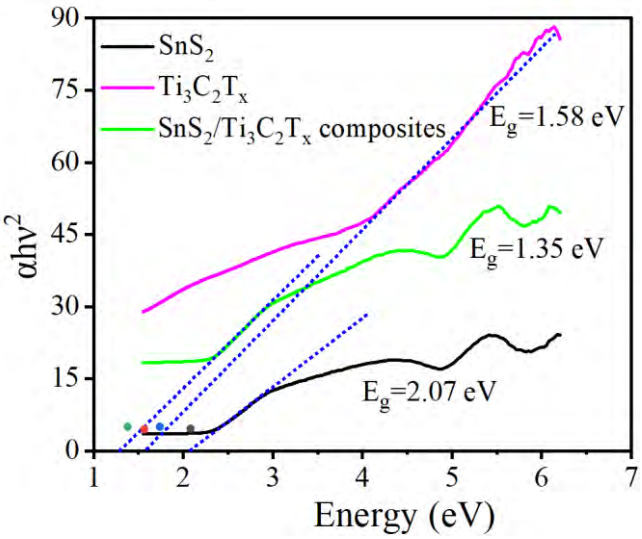

Fig. S6. The band gaps were calculated by the Tauc plot equation based on the UV−vis absorption spectra of SnS_2, $Ti_3C_2T_x$ and composites (Sn-Ti-b).

Table S1. Comparison of NH_3-sensing performance of $SnS_2/Ti_3C_2T_x$ composites in this work with those in the previous work.

Sensing materials	**concentration (ppm)**	**Response/recovery time (s)**	**Temperature (℃)**	**Response (%)**	**Ref.**
$Ti_3C_2T_x$	100	300/900	RT	0.8	[34]
$Ti_3C_2T_x$	500	-/-	RT	6.13	[35]
V_2CT_x	100	300/400	RT	1.66	[36]
SnS_2 nanoflower	100	40.6/624	200	86.48	[11]
SnS_2 micro-flowers	50	4/15	160	89.58	[12]
SnO_2/SnS_2	10	11/-	116	1.16	[37]
$Ti_3C_2T_x/TiO_2$	10	60/750	RT	3.1	[38]
$PANI/Ti_3C_2T_x$	10	240/490	RT	1.65	[39]
$SnS_2/Ti_3C_2T_x$	100	116/521	RT	61.36	This work

Additionally, a similar work has been published titled with "Engineering a surface functionalized Pt@SnS_2/$Ti_3C_2T_x$ MXene sensor with humidity tolerance and high sensitivity at room temperature for NH_3 detection" (J. Mater. Chem. A, 2025, 13,2950-2964). And the authors did not present a different or novelty of the problem they are studying in the introduction. Many previous references have already reported similar results.

Answer: Thanks for the reviewer's good suggestion. The difference between this work and other previous work is showing following:

(1) The effect of $Ti_3C_2T_x$ content on the NH_3-sensing performance of SnS_2/$Ti_3C_2T_x$ composites has been studied in this work. In the previous work, the ternary heterostructure of Pt@SnS_2/$Ti_3C_2T_x$ has been prepared and behaved excellent room-temperature NH_3-sesning performance. While, the optimum content of composition ratio was not researched. Hence, in this paper, the effect of $Ti_3C_2T_x$ content on the NH_3-sensing performance of SnS_2/$Ti_3C_2T_x$ composites was mainly studied. It's found that the NH_3-sensing response increases as the $Ti_3C_2T_x$ content is increased from 0 to 0.4 *wt*% but decreases thereafter. The composites with 0.4 *wt*% $Ti_3C_2T_x$ behave the optimum NH_3-sensing response at RT.

(2) The selectivity mechanism of SnS_2/$Ti_3C_2T_x$ composites have been studied in this paper. To revel the selectivity mechanism of SnS_2 and $Ti_3C_2T_x$ composites toward NH_3 molecular, the adsorption energy of SnS_2 toward NH_3, acetone, ethanol, H_2S, H_2, methanol and SO_2 was calculated. It's found that the adsorption energy of SnS_2 toward NH_3 is much more negative that of SnS_2 toward other gases, indicating the

stronger adsorption ability to NH_3 molecular. Hence, fabrication of SnS_2 and $Ti_3C_2T_x$ composites show the excellent selectivity to NH_3 gas molecular.

(3) ***According to the results of in situ DRIFTS, it's found that the NO_2 is generated in the process of NH_3-sensing response.*** The results of in situ DRIFTS is shown in Figure S2. The peaks at 1,070 cm^{-1} and 1,563 cm^{-1} are related to N−H bonds coupled to Lewis acid sites, while those at 1,506 cm^{-1}, 1,539 cm^{-1}, and 1,693 cm^{-1} are associated with NH_4^+ chemisorbed at Brønsted acid sites. The Lewis and Brønsted acid sites have strong adsorption ability toward alkaline NH_3. The strong peaks at about 1,624 cm^{-1} and 1,693 cm^{-1} correspond to adsorbed NO_2, indicating that NO_2 is generated in the gas-sensing process.

The following reference has been added in the revised manuscripr:

[20] K. S. Ranjith, S. Sonwal, A. Mohammadi, G. S. R. Raju, Y. S. Huh, Y. K. Han, Engineering a surface functionalized Pt@SnS_2/$Ti_3C_2T_x$ MXene sensor with humidity tolerance and high sensitivity at room temperature for NH_3 detection, J. Mater. Chem. A, 13 (2025) 2950-2964.

What is the superiority of this new SnS_2 nanosheets functionalized $Ti_3C_2T_x$?

Answer: Thanks for the reviewer's good suggestion. The superiorities of this new SnS_2 nanosheets functionalized $Ti_3C_2T_x$ are shown in following:

(1) The SnS_2 show the hexagonal structure. When composited with $Ti_3C_2T_x$, the SnS_2 nanosheets on $Ti_3C_2T_x$ could inhibit restacking of SnS_2 and oxidation of $Ti_3C_2T_x$. The $Ti_3C_2T_x$ serves as template for growth of SnS_2 nanosheets and generates interfacial sites for NH_3 gas adsorption. Hence, the NH_3-sensing performance is enhanced.

(2) When SnS_2 is contacted with $Ti_3C_2T_x$, the heterojunction is formed at interface. It would increase the lifetime of electron, promoting the electron exchange between NH_3 molecular and sensing materials and enhancing NH_3-sensing response.

(3) Based on the results of DOS and PDOS, it's found that the pure SnS_2 show the semiconductor property. The $Ti_3C_2T_x$ show the metal property. When the heterojunction of SnS_2 and $Ti_3C_2T_x$ is formed, the bandgap is zero, behaving the metal property. Hence, fabrication of SnS_2 and $Ti_3C_2T_x$ composites could enhance the conductivity.